*mathematics*

*Article*

# Analysis of Stress and Deformation on Surrounding Rock Mass of a Trapezoidal Roadway in a Large Inclination Coal Seam and Novel High Yielding Prop Support: A Case Study

**Yang Hao [1,2,3,*], Chunhui Liu [2], Yu Wu [1,2,*], Hai Pu [1,2], Kai Zhang [1,2] and Lingling Shen [3]**

[1] State Key Laboratory for Geomechanics and Deep Underground Engineering, China University of Mining and Technology, Xuzhou 221116, China
[2] School of Mechanics and Civil Engineering, China University of Mining and Technology, Xuzhou 221116, China
[3] School of Mines, China University of Mining and Technology, Xuzhou 221116, China
* Correspondence: yanghao@cumt.edu.cn (Y.H.); wuyu@cumt.edu.cn (Y.W.); Tel.: +86-13852082572 (Y.W.)

**Abstract:** Trapezoidal roadways in large inclination coal seams show asymmetrical tectonic characteristics, while there is still a lack of theoretical results on stress, deformation, and efficient and effective supporting methods on high walls. In this paper, based on the geological characteristics of a large, inclined coal seam roadway, a mechanical model for stress–deformation analysis of trapezoidal section roadway was established. Complex analysis and a comfort map were employed to investigate the stress and deformation distribution on the roadway surface, and a novel yielding prop with high load capacity and constant working resistance was employed to support a high wall side based on analytical results. The results are as follows: (1) The deformation of the high wall is larger than that of the low wall, and the deformation of the roof is larger than that of the floor. The overall deformation of the surrounding rock shows that the rib closure is larger than the roof-to-floor closure. (2) The stress of the surrounding rock shows that both horizontal and vertical stresses are highest in the upper corner, indicating that the broken zone is most likely to occur at this location. (3) A new support employed with a high-yielding prop and a high-strength cable in a large, inclined angle roadway is proposed. On-site experiments were conducted in a large 5-1081 roadway of a coal mine in Shanxi, China. Under the influence of mining disturbance, the deformations at the top corner decreased by 40% compared with before. The test results show that the new support scheme can effectively control the development of roadway deformation and damage during the mining process. The new support also shows friendly environmental support and fast installation.

**Keywords:** large inclination coal seam; trapezoidal roadway; failure mechanism; yielding prop supporting; case study

**MSC:** 86-05; 86-08



**Citation:** Hao, Y.; Liu, C.; Wu, Y.; Pu, H.; Zhang, K.; Shen, L. Analysis of Stress and Deformation on Surrounding Rock Mass of a Trapezoidal Roadway in a Large Inclination Coal Seam and Novel High Yielding Prop Support: A Case Study. *Mathematics* **2023**, *11*, 319. https://doi.org/10.3390/math11020319

Academic Editors: Lev Levin and Mikhail Semin

Received: 12 November 2022
Revised: 31 December 2022
Accepted: 4 January 2023
Published: 7 January 2023



## 1. Introduction

With the rapid development of China's economy, coal has gradually become a strategic energy source to support China's sustained economic growth and play a leading role in economic development. According to statistics, among the graded coal mines in China, the large inclination coal seam accounts for about one-sixth of the total coal mines, and the reserves with coal seam inclination above 35° account for about 17%, especially in a southeast coastal area, the large inclination coal seam mines account for about 60% [1]. Although the reserves of large, inclined coal seams are less than 20% of the total coal reserves in the western region [2–4], the high-quality coal is quite prevalent, and accounts for 85% [4,5].

The roadway stability control of large, inclined coal seams is an important prerequisite for ensuring the safety of mines [5–7]. At present, there is no unified definition of the concept of large inclination. It is generally considered that a large inclination coal seam is a coal seam inclination angle between 25° and 55° [8–11]. Due to the influence of coal seam inclination, the angle between the coal rock lamina direction and rock seam gravity direction becomes smaller. The force of rock seam gravity along the lamina direction is greatly increased, which shows different surrounding rock damage characteristics compared to a horizontal coal seam. After roadway excavation, affected by the geological structure and disturbance pressure, the stress distribution on the top and bottom surrounding rocks and the two ribs are uneven. The surrounding rock slips along the direction of the laminae, and the top and bottom rocks' deformation damage problem are dramatically asymmetrical, especially when the strength difference between the top and bottom increases. It is difficult for conventional support to effectively control the harmful deformation of such roadways. Usually, the support cost of a large, inclined coal seam roadway is about 30% higher than that of a near-horizontal roadway [12–14]. If the deformation and damage mechanism of the roadway surrounding the rock is not understood, and the support parameters are designed blindly, the roadway will have serious destabilization damage, which directly threatens the roadway safety and brings significant economic loss to the coal mine. Therefore, the failure mechanism and control technology of large, inclined coal seam roadways surrounding rock is significant to ensure the safety of large inclined coal seams [15,16].

There are many innovative studies involving rock failure prediction and rock properties related to micro–macro aspects. The mechanical and mathematical model involves phase-field fracture problems employed by Bayesian estimation [17], a plastic-strain-induced damage model of porous rock suitable for different stress paths combined with statistical damage mechanics, and a series of conventional tri-axial compressive experiments [18], such as experimental tests to investigate the stress relaxation behavior of marble under cyclic weak disturbance and confining pressures [19], the micro investigation on shale characteristics, gas contents related to buried depth, organic origins, and regional analysis [20]. The integrated research on the mineralogical, geochemical, and stable isotope characteristics of the Upper Triassic high-sulfur coals from the Khanh Hoa open-pit mine, Thai Nguyen Coalfield, NE Vietnam was analyzed by SEM and optical photomicrographs [21]. This research encourages more studies related to the micro–macro relationship. While in the aspect of field application, the macro aspects of rock failure are still a major problem to be concerned about, especially for trapezoidal roadways in large, inclined coal seams. The asymmetrical characteristics show deformation, stress distribution, plastic zone, and rib spalling [22–25]. In some cases, the roof and floor were more fragile due to the soft rock, and the separation of the bedded structural roof at different depths [5,26–28]. However, the cross-section, in that case, is rectangular. In large inclination coal seams, trapezoidal section roadways are common on site due to their conventional and fast excavation. However, the mechanical interpretation of the stress and deformation of the roadway is still difficult, and fast, efficient, safe, and environmentally friendly control technology still needs to be improved.

In this paper, mechanical and mathematical modeling of trapezoidal roadways on large inclination coal seams are employed to solve analytical solutions on stress and deformation. Based on the analytical results, a novel high-yielding prop was employed to examine the supporting effect. An on-site supporting experiment on a large, inclined coal seam roadway was put forward to verify the analytical results and to test the effect on the high-yielding prop. The research results can provide a theoretical and practical basis for the design of roadway support for large, inclined coal seams, and are of great significance for solving the engineering problems of large inclined coal seam mining.

## 2. Geological Background

The roadway excavated on a large inclination coal seam was selected at the 5-1081 roadway in a coal mine located in Shanxi, China. The working face elevation is about +385 m~+550 m. The schematic diagram of the working surface is shown in Figure 1a. The 5-1081 roadway is a trapezoidal section with a width of 5.0 m, a low height of 2.0 m, a high height of 4.9 m, and a roof inclination of 30°. Steel band, cable, and rock bolt support are adopted, with a φ22 mm × 2400 mm left-hand threaded steel high-strength rock bolt at the top and a φ20 mm × 2000 mm left-hand threaded steel high-strength anchor rod at the gang, with the distance between rows of anchor rods being 800 mm × 800 mm. A φ21.8 mm × 8300 mm anchor rope is used at the top, with the distance between rows being 1600 mm × 3200 mm in a group of three. The section parameters of the roadway support are shown in Figure 1b.

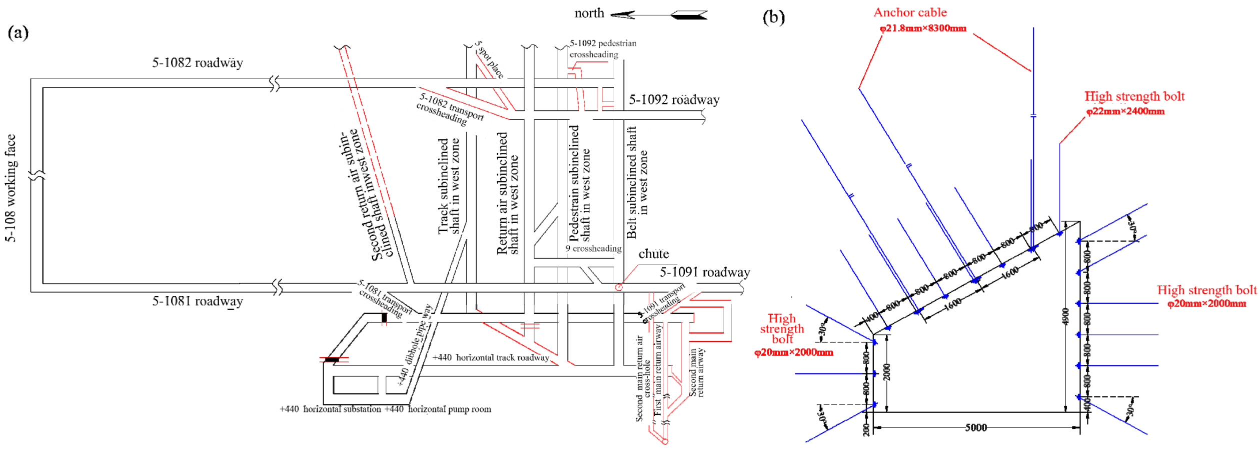


**Figure 1.** Layout of rock bolt supporting method: (**a**) schematic diagram; (**b**) cross-section diagram.

The dip angle of the mining coal seam named 5# is 25~34°, average of 30°. The average thickness of the 5# coal seam is about 6.1 m, in which the crack and joints on the coal seam are developed. The structure of the coal seam is complex. In the middle of the coal seam, it is sandwiched between two layers of carbonaceous rock and mudstone. The thickness of the coal seam does not change much, it is a more stable coal seam, and the total thickness of the gangue is about 1.3 m. Most of the lithology is carbonaceous mudstone, and there is a small amount of local mudstone, due to the mudstone Platts hardness $f = 2$. The direct roof is mudstone with an average thickness of 1.43 m, the upper roof is sandy mudstone with an average thickness of 2.28 m, the direct floor is sandstone with an average thickness of 1.2 m, and the old bottom is mudstone with an average thickness of 2.1 m. The comprehensive geological column diagram of the working face is shown in Figure 2. In the coal seam, the faults are developed to different degrees. The largest fault drop is 4.5 m, and the smallest fault drop is 0.5 m. The 5–1081 face is mainly affected by six faults, among which three faults, F7, F8, and F9, have effects on the mining process.

According to geo-stress tests, the maximum horizontal stress of the roadway is about 6.56 MPa and the vertical stress is about 8.25 MPa, which can be regarded as being in a state of uniform pressure of 7.41 MPa. From the results of the rock mechanics parameter test shown in Figure 3, it is known that the elastic modulus of the sandstone is 3.5 GPa and Poisson's ratio is 0.24. The uniaxial compress strength of sandstone, limestone, and mudstone are 40.55 MPa, 117.56 MPa, and 54.93 MPa, respectively.

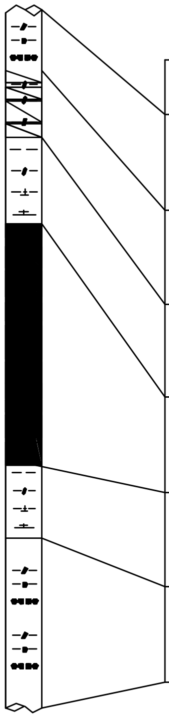

| Lithology | depth (m) | Layer thickness(m) |
|---|---|---|
| Sandstone | 509.56 | 2.17–15.40 / 4.5 |
| Sandy mudstone | 515.84 | 1.50–3.80 / 2.28 |
| Mudstone | 517.24 | 2–23.68 / 1.43 |
| 5#coal | 520.68 | 5.55–24.20 / 6.1 |
| Sandstone | 522.93 | 1.5–9.87 / 1.2 |
| Mudstone | 524.57 | 3.7–42.17 / 2.1 |

**Figure 2.** Comprehensive geological histogram.

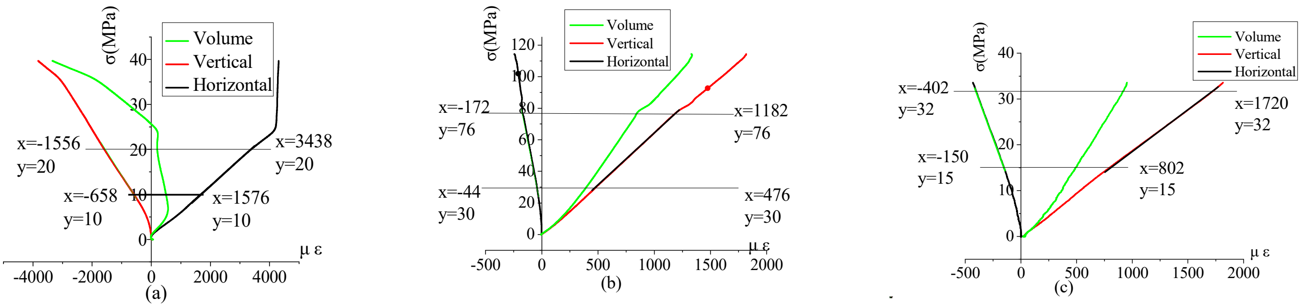


**Figure 3.** Stress−strain curve of (**a**) sandstone, (**b**) limestone, (**c**) mudstone in 5# coal seam.

## 3. Mechanics Analysis of Surrounding Rocks Stress Distribution and Deformation in Deeply Inclined Coal Seam Roadway

The deformation and stress distribution of roadway rocks are the basis for its supporting design. At present, mechanical analysis of the roadway simplifies the section into a circle. Since the actual roadway form does not match, the results can only be used as a qualitative reference. Some scholars have also analyzed the stress distribution of a rectangular cross-section using the method of complex analysis and conformal map [29], but the results do not apply to trapezoidal roadways with large inclinations. This section uses the method of complex analysis and conformal map to convert the trapezoidal roadway into a circle and derives the formula on the stress and displacement of the surrounding rocks of the trapezoidal roadway.

### *3.1. Mechanical Modeling*

Before the analysis of deformation and stress distribution on the surrounding rocks, some assumptions should be made. First, the excavation is long enough to consider that plane strain conditions apply in any cross-section. Secondly, the surrounding rock is continuous, homogeneous, isotropic, and linearly elastic.

According to the geometric characteristics of the large inclination roadway, it is simplified to a trapezoidal orifice problem in an infinite plane, as shown in Figure 4a. The uniform load $P$ is applied on the upper side of the overlying rock seam. The left and right boundary conditions are hinge support constraints. The bottom side of this model is a fixed constraint. The short height of the trapezoidal roadway is $a$, the width is $b$, and the coal seam inclination angle is $\theta'$. The balanced state is redistributed after excavation. The analysis domain is extracted from the infinite plane, and the geometric is set as ten times the width and height of the trapezoidal roadway. The stress boundary condition is set as the initial geo-stress shown in Figure 4b. The boundary condition on the surface of the trapezoidal roadway was assumed as normal stress and tangential stress-free.

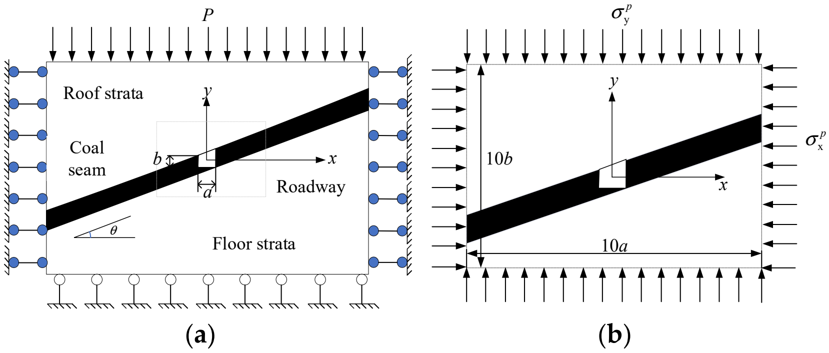


**Figure 4.** Mechanical modeling of trapezoidal roadway.

### *3.2. Flow Chart on Stress and Strain Calculation Based on Complex Analysis and Comfort Mapping*

As shown in Figure 5, the complex analysis of Cartesian coordinates into Polar coordinates is used $z = \omega(\zeta)$. In the $\zeta$ plane, such that:

$$\zeta = \rho(\cos\theta + i\sin\theta) = \rho e^{i\theta} \tag{1}$$

where $\rho$ and $\theta$ are the polar coordinates of the point $\zeta$. A circumference in the $\zeta$ plane $\rho = \text{const.}$ and a radial line $\theta = \text{const.}$ $i$ is the imaginary number. Due to the angle-preserving nature of the transformation, the two sets of curves are always orthogonal and the corresponding tangents $\rho$, $\theta$ are called curve axes and their relative directions are the same as the coordinate axes $x$ and $y$.

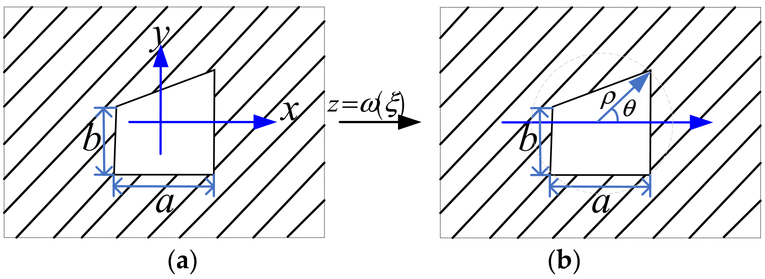


**Figure 5.** Conformal mapping from the trapezoidal roadway to the circle plane: (**a**) $z$ plane; (**b**) $\zeta$ plane.

Let there be a vector $F$ in the $z$-plane, in which the points start $z = \omega(\zeta) = \omega(\rho e^{i\theta})$. $F_x$ and $F_y$ are the projections of this vector on the $x$ and $y$ axes, $F_\rho$ and $F_\theta$ are the projection of $\rho$ and $\theta$. Assuming that the angle between axial $\rho$ and $\theta$ is $\lambda$, the geometric relationship is as follows:

$$\begin{aligned} F_x &= F_\rho\cos\lambda - F_\theta\sin\lambda z = \omega(\zeta) \\ F_y &= F_\rho\sin\lambda + F_\theta\cos\lambda \end{aligned} \tag{2}$$

Rearranging Equation (2), it can be transformed into:

$$\begin{aligned} F_x + iF_y &= (F_\rho + iF_\theta)e^{i\lambda} \\ F_\rho + iF_\theta &= (F_x + iF_y)e^{-i\lambda} \end{aligned} \tag{3}$$

To find $e^{-i\lambda}$, assuming a displacement increment dz in $\rho$ axial; thus, the corresponding point $\zeta$ has radial displacement $d\zeta$, and $\mathrm{d}z = e^{i\lambda}|\mathrm{d}z|$, $\mathrm{d}\zeta = e^{i\theta}|\mathrm{d}\zeta|$.

Therefore, $e^{-i\lambda}$ can be rearranged:

$$e^{i\lambda} = \frac{\mathrm{d}z}{|\mathrm{d}z|} = \frac{\omega'(\zeta)\mathrm{d}\zeta}{|\omega'(\zeta)| \cdot |\mathrm{d}\zeta|} = e^{i\theta}\frac{\omega'(\zeta)}{|\omega'(\zeta)|} = \frac{\zeta}{\rho}\frac{\omega'(\zeta)}{|\omega'(\zeta)|} \tag{4}$$

The two sides of the above equation are taken to be conjugates, i.e., $e^{-i\lambda}$, Equation (3) is rearranged:

$$F_\rho + iF_\theta = \frac{\overline{\zeta}}{\rho}\frac{\overline{\omega'(\zeta)}}{|\omega'(\zeta)|}\left(F_x + iF_y\right) \tag{5}$$

in which the underscore denotes the conjugate of function.

The equation of displacement $\boldsymbol{u}$ and stress $\boldsymbol{\sigma}$ is derived as follows:

First transform the function related to $z$ into a function related to $\zeta$:

$$\begin{aligned} \varphi(\zeta) &= \varphi_1(z) = \varphi_1[\omega(\zeta)] \\ \psi(\zeta) &= \psi_1(z) = \psi_1[\omega(\zeta)] \end{aligned} \tag{6}$$

$$\begin{aligned} &\Phi(\zeta) = \varphi_1'(z) = \varphi'(\zeta)/\omega'(\zeta) \\ &\Psi(\zeta) = \psi_1'(z) = \psi'(\zeta)/\omega'(\zeta) \\ &\Phi'(\zeta) = \varphi_1''(z) \cdot \omega'(\zeta) \end{aligned} \tag{7}$$

Then, substitute Equation (7) into Equation (1) to obtain:

$$\frac{E}{1+\nu}(u + iv) = \frac{3-\nu}{1+\nu}\phi(\zeta) - \frac{\omega(\zeta)}{\overline{\omega'(\zeta)}}\overline{\phi'(\zeta)} - \overline{\psi(\zeta)} \tag{8}$$

in which $\nu$ = 3–4 $\mu$ in plain strain problem, $\mu$ is Poisson's ratio.

Run the projections of the displacement vector $u_\rho$ and $u_\theta$ on the $\rho$ and $\theta$ axes, respectively, then Equation (5) is:

$$u_\rho + iu_\theta = \frac{\overline{\zeta}}{\rho}\frac{\overline{\omega'(\zeta)}}{|\omega'(\zeta)|}(u + iv) \tag{9}$$

Then, substitute Equation (8) into Equation (9) to obtain the complex potential representation of the displacement component of the curve coordinates:

$$\frac{E}{1+\nu}(u_\rho + iu_\theta) = \frac{\overline{\zeta}}{\rho}\frac{\overline{\omega'(\zeta)}}{|\omega'(\zeta)|}\left[\frac{3-\nu}{1+\nu}\varphi(\zeta) - \frac{\omega(\zeta)}{\overline{\omega'(\zeta)}}\overline{\varphi'(\zeta)} - \overline{\psi(\zeta)}\right] \tag{10}$$

Assuming that $\sigma_\rho\sigma_\theta\tau_{\rho\theta}$ is the stress component of an elastic body in the curve coordinates $\rho$ and $\theta$, using the coordinate transformation relationship we obtain:

$$\begin{aligned} &\sigma_\theta + \sigma_\rho = \sigma_y + \sigma_x, \\ &\sigma_\theta - \sigma_\rho + 2i\tau_{\rho\theta} = (\sigma_y - \sigma_x + 2i\tau_{xy})e^{2i\lambda} \end{aligned} \tag{11}$$

Substituting Equation (10) into Equation (4), we have:

$$\begin{aligned} &\sigma_\theta + \sigma_\rho = 4\mathrm{Re}\varphi_1'(z), \\ &\sigma_\theta - \sigma_\rho + 2i\tau_{\rho\theta} = 2\left[\overline{z}\varphi_1''(z) + \psi_1'(z)\right]e^{2i\lambda} \end{aligned} \tag{12}$$

In addition:

$$
\begin{aligned}
&e^{2i\lambda} = \frac{\zeta^2\omega'^2(\zeta)}{\rho^2|\omega'(\zeta)|^2} = \frac{\zeta^2\omega'^2(\zeta)}{\rho^2\omega'(\zeta)\overline{\omega'(\zeta)}}\\
&\sigma_\theta + \sigma_\rho = 4\mathrm{Re}\Phi(\zeta)\\
&\sigma_\theta - \sigma_\rho + 2i\tau_{\rho\theta} = \frac{2\zeta^2}{\rho^2\overline{\omega'(\zeta)}}\left[\overline{\omega(\zeta)}\Phi'(\zeta) + \omega'(\zeta)\Psi(\zeta)\right]
\end{aligned} \tag{13}
$$

From the elastic mechanics, it is known that the complex variable function of the stress and deformation of surrounding rocks is mainly determined by two analytic functions, $\varphi(\zeta)$, $\psi(\zeta)$. The basic equations for stress and deformation are as follows:

$$
\begin{aligned}
&\sigma_\rho + \sigma_\theta = 2[\Phi(\zeta) + \overline{\Phi(\zeta)}\ ] = 4\mathrm{Re}\Phi(\zeta)\\
&\sigma_\rho - \sigma_\theta + 2i\tau_{\rho\theta} = \frac{2\zeta^2}{\rho^2\ \overline{\omega(\zeta)}}[\ \overline{\omega(\zeta)}\ \Phi(\zeta) + \omega(\zeta)\Psi(\zeta)]\\
&2G(u_\rho + iu_\theta) = \frac{\bar{\zeta}}{\rho}\frac{\omega(\zeta)}{|\omega(\zeta)|}[\tfrac{3-u}{1+u}\varphi(\zeta) - \frac{\omega(\zeta)}{\omega(\zeta)}\varphi(\zeta) - \psi(\zeta)]
\end{aligned} \tag{14}
$$

in which:

$$
\begin{aligned}
&\begin{cases}
\varphi(\zeta) = \frac{1+u}{8\pi}(x+iy)\ln\zeta + B\omega(\zeta) + \varphi_0(\zeta)\\
\psi(\zeta) = -\frac{3-u}{8\pi}(x-iy)\ln\zeta + (B+iC)\omega(\zeta) + \psi_0(\zeta)
\end{cases}\\
&\begin{cases}
\Phi(\zeta) = \frac{\varphi(\zeta)}{\omega(\zeta)}\\
\Psi(\zeta) = \frac{\psi(\zeta)}{\omega(\zeta)}
\end{cases}\\
&\begin{cases}
B = \frac{1}{4}(\sigma_y + \sigma_x)\\
B = \frac{1}{4}(\sigma_y - \sigma_x)\\
C = \tau_{xy}\\
B + iC = -\frac{1}{2}(\sigma_1 - \sigma_2)e^{-2i\alpha}
\end{cases}
\end{aligned} \tag{15}
$$

where $\alpha$ is the principal stress direction.

$\varphi_0(\zeta) = \sum\limits_{n=1}^{\infty}\alpha_n\zeta^{-n}$ and $\psi_0(\zeta) = \sum\limits_{n=1}^{\infty}\beta_n\zeta^{-n}$ within the circle are the analytical function of a complex variable $\zeta$. They are continuous within and around the circle. The basic formula can be expressed as:

$$
\begin{aligned}
&\varphi_0(\zeta) + \frac{1}{2\pi i}\int_\sigma \frac{\omega(\sigma)}{\overline{\omega(\sigma)}}\frac{\overline{\varphi_0(\zeta)}}{\sigma-\zeta}d\sigma = \frac{1}{2\pi i}\int_\sigma \frac{f_0 d\sigma}{\sigma-\zeta}\\
&\psi_0(\zeta) + \frac{1}{2\pi i}\int_\sigma \frac{\overline{\omega(\sigma)}}{\omega(\sigma)}\frac{\varphi_0(\zeta)}{\sigma-\zeta}d\sigma = \frac{1}{2\pi i}\int_\sigma \frac{\overline{f}_0 d\sigma}{\sigma-\zeta}
\end{aligned} \tag{16}
$$

in which:

$$
f_0 = i\int(\overline{x} + i\overline{y})ds - \frac{x+iy}{2\pi}\ln\sigma - \frac{1+\mu}{8\pi}(x-iy)\frac{\omega(\sigma)}{\omega(\sigma)}\sigma - 2B\omega(\sigma) - (B-iC)\overline{\omega(\sigma)} \tag{17}
$$

Complex variables $\zeta$ are generally expressed as:

$$
\zeta = \rho e^{i\theta} \tag{18}
$$

According to Riemann's theorem, the mapping function of any hole exists. According to the theory of complex functions, the basic form of the function that maps the outer domain of a trapezoidal section alleyway to the circle can be written in the hierarchical form:

$$
Z = \omega(\zeta) = C_0 + C_1\zeta + C_2\zeta^{-1} + C_3\zeta^{-2} + \ldots\ldots + C_m\zeta^{-m+1} \tag{19}
$$

where $C_j(j = 1, 2, \ldots\ldots, m)$ is the common plural, $m$ is several level items $C_0$, and is only related to the coordinate origin of the alleyway selection.

Transform Equation (19) to obtain:

$$z = \omega(\zeta) = C_0 + C_1(\zeta + B_1\zeta^{-1} + B_2\zeta^{-2} + \ldots\ldots + B_m\zeta^{-m}) \tag{20}$$

According to the Theory of Complex Functions, when mapping the external domain of the alley to the circle, $C_1$ is only related to the size of the hole, while $B_j$ is only related to the shape of the hole. In general $C_1$, $B_j$ are plural.

For the convenience of calculation:

$$C_j = a_j + id_j \tag{21}$$

For a point around the perimeter of the lane, mapped onto the unit circle, the complex variable becomes:

$$\zeta = \sigma = e^{i\theta} \tag{22}$$

According to Equations (19)–(21), the mapping function becomes:

$$z = x + iy = a_0 + id_0 + (a_1 + id_1)e^{i\theta} + \sum_{j=2}^{m} (a_j + id_j)e^{-i(j-1)\theta} \tag{23}$$

Comparing Equations (20) and (23), it can be concluded:

$$\begin{cases} C_0 = a_0 + id_0 \\ C_1 = a_1 + id_1 \\ C_1 B_{j-1} = a_j + id_j, (j = 2, 3, \ldots\ldots, m) \end{cases} \tag{24}$$

By separating the real part and the imaginary part of Equation (23), the expression of the coordinates of the points around the perimeter of the roadway can be obtained:

$$\begin{cases} x = a_0 + a_1\cos\theta - d_1\sin\theta + \sum\limits_{j=2}^{m} [a_j\cos(j-1)\theta + d_j\sin(j-1)\theta] \\ y = d_0 + a_1\sin\theta + d_1\cos\theta + \sum\limits_{j=2}^{m} [-a_j\sin(j-1)\theta + d_j\cos(j-1)\theta] \end{cases} \tag{25}$$

Equation (25) can be obtained as follows:

$$\begin{cases} a_0 = \frac{1}{2\pi}\int_0^{2\pi} xd\theta \\ d_0 = \frac{1}{2\pi}\int_0^{2\pi} yd\theta \\ a_1 = \frac{1}{2\pi}\int_0^{2\pi} (x\cos\theta + y\sin\theta)d\theta \\ d_1 = \frac{1}{2\pi}\int_0^{2\pi} (y\cos\theta - x\sin\theta)d\theta \\ a_j = \frac{1}{2\pi}\int_0^{2\pi} [x\cos(j-1)\theta - y\sin(j-1)\theta]d\theta \\ d_j = \frac{1}{2\pi}\int_0^{2\pi} [y\cos(j-1)\theta + x\sin(j-1)\theta]d\theta \end{cases} \\ (j = 2, 3, \ldots\ldots, m) \tag{26}$$

The boundary condition is as the mathematical form:

$$\begin{cases} \sigma_x(x = \pm 5a) = \sigma_x^p \\ \sigma_y(y = \pm 5b) = \sigma_y^p \end{cases} \begin{cases} \sigma_\rho(s) = 0 \\ \tau_{\rho\theta}(s) = 0 \end{cases} \tag{27}$$

where $s$ is the inner surface of the trapezoidal roadway.

The iterative flow chart of analytical solutions on stress and deformation is shown in Figure 6. First, a point on the original lane $(x, y)$ assumes a mapping correspondence, which can be given arbitrarily, according to which this point is mapped to the unit circle with the image point $(\rho, \theta)$. The first approximation of the coefficients of the mapping function is obtained by mapping the entire alleyway perimeter points and solving according to Equation (26). Substituting the obtained coefficients into Equation (25), the coordinates of the points around the alleyway are obtained $(x, y)$, and the relationship between $(\rho, \theta)$ and $(x, y)$ is $(x, y)$. Then, solve the value of the improved coefficients by Equation (26), and then substitute them into Equation (25), and so on iteratively until the resulting roadway cross-section shape is close enough to the original roadway shape. The coordinates of the points $s$ evenly distributed on the surface of the roadway can be expressed as $({x_q}^0, {y_q}^0)$. Likewise, the unit circle has a uniform distribution of pixels, whose coordinates s can be expressed as $(\rho, \theta_q, q = 1 \sim s)$. When $s$ is large enough, the coordinates of the line segment divided by two adjacent points on the perimeter of the lane can be considered constant and equal to the average of the coordinates of the two ends, i.e.,

$$\begin{cases} \bar{x_q}^0 = \frac{{x_q}^0 + {x_{q+1}}^0}{2} \\ \bar{y_q}^0 = \frac{{y_q}^0 + {y_{q+1}}^0}{2} \end{cases} \tag{28}$$

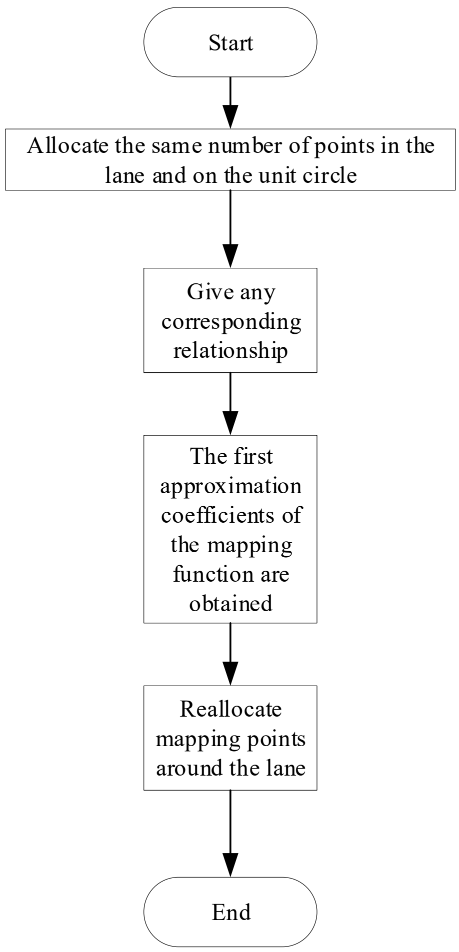


**Figure 6.** Iterative flow chart.

Then, the segmental integral can be approximated as the summation. Equation (26) becomes:

$$\begin{cases} a_0{}^1 = \frac{1}{2\pi}\sum\limits_{q=1}^{s} \bar{x_q}^0 \\ d_0{}^1 = \frac{1}{2\pi}\sum\limits_{q=1}^{s} \bar{y_q}^0 \\ a_1{}^1 = \frac{1}{2\pi}\sum\limits_{q=1}^{s} [\bar{x_q}^0(\sin\theta_{q+1} - \sin\theta_q) - \bar{y_q}^0(\cos\theta_{q+1} - \cos\theta_q)] \\ d_1{}^1 = \frac{1}{2\pi}\sum\limits_{q=1}^{s} [\bar{y_q}^0(\sin\theta_{q+1} - \sin\theta_q) + \bar{x_q}^0(\cos\theta_{q+1} - \cos\theta_q)] \\ a_j{}^1 = \frac{1}{2\pi}\sum\limits_{q=1}^{s} [\bar{x_q}^0(\sin j\theta_{q+1} - \sin j\theta_q) + \bar{y_q}^0(\cos j\theta_{q+1} - \cos j\theta_q)] \\ d_j{}^1 = \frac{1}{2\pi}\sum\limits_{q=1}^{s} [\bar{y_q}^0(\sin j\theta_{q+1} - \sin j\theta_q) - \bar{x_q}^0(\cos j\theta_{q+1} - \cos j\theta_q)] \end{cases}$$
$$(j = 2, 3, \ldots\ldots, m) \tag{29}$$

After calculation, the approximate coefficients of the mapping function obtained by Equation (29) are substituted into Equation (25), and according to the correspondence between the requested alleyway and the unit circle, the mapping points corresponding to the projection on the alleyway reflected by the image points marked on the unit circle can be obtained, and these points are unevenly distributed on the periphery. The distance between two adjacent points is recorded in turn and redistributed according to the distance between the mapped points on the perimeter of the requested lane, then the coordinates of the points on the requested lane are marked as $(x_q{}^1, y_q{}^1)$. The corresponding image point is still $(\rho, \theta_q)$. Substituting $(x_q{}^1, y_q{}^1)$ into Equations (28) and (29) obtain each coefficient $a_j{}^2 d_j{}^2$ and iterate until the exact value is obtained.

### 3.3. Results

Based on the above analysis, substituting the geo-stress state of $\sigma_x$ and $\sigma_y$ as 7.41 MPa, obtains the surface of the roadway as the elastic state. The elastic modulus and Poisson's ratio are set as 3.5 GPa and 0.3, respectively. The coordinates of the points s evenly distributed on the surface of the roadway are shown in Figure 7.

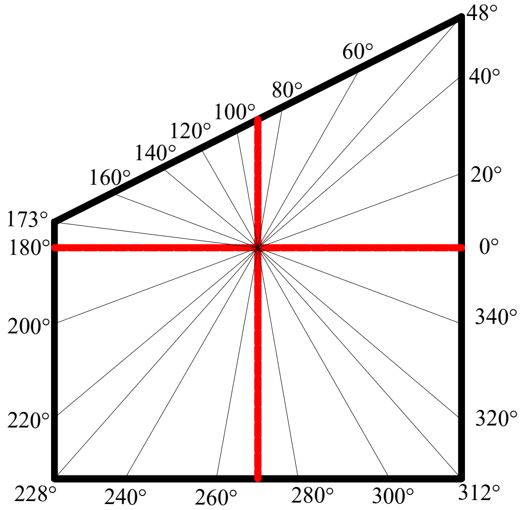


**Figure 7.** Layout of roadway azimuth.

The boundary conditions on the surface of the roadway must be $\sigma_n = 0$, $\tau_{nt} = 0$, where $n$ is normal, and $t$ is tangent to the contour. The stress $\sigma_t$ will be found using the future solution. In particular, there should be $\sigma_x = 0$, $\tau_{xy} = 0$, on the two side walls, and $\sigma_y = 0$, $\tau_{yx} = 0$ on the horizontal floor.

### 3.3.1. Deformation Characteristics

The calculation deformation results are shown in Table 1 and Figure 8. From Table 1, the maximum horizontal displacement occurs in the position of 0° and 180°, in the two ribs. This indicates that the spalling rib may occur after excavation. The maximum displacement of the right rib is 12.32 mm, and the maximum displacement of the left rib is 10.86 mm, so rib closure is about 23.18 mm; in addition, the maximum vertical displacement of the roadway occurs in the position of 100° and 260°, on the top and bottom plate, respectively. The maximum sinking of the roof is about 34 mm. The overall deformation of the surrounding rock shows that the characteristics of roof-to-floor deformation are larger than rib closure.

**Table 1.** Displacement results.

| Angle | Horizontal Displacement/mm | Vertical Displacement/mm | Total Displacement/mm |
|---|---|---|---|
| 0° | −10.86 | −1.46 | 10.96 |
| 20° | −7.62 | −2.71 | 8.09 |
| 40° | −6.51 | −3.24 | 7.27 |
| 48° | −5.63 | −5.21 | 7.67 |
| 60° | −1.31 | −12.35 | 12.42 |
| 80° | −2.22 | −12.37 | 12.57 |
| 100° | 2.48 | −26.12 | 26.24 |
| 120° | 2.67 | −19.23 | 19.41 |
| 140° | 5.56 | −17.21 | 18.09 |
| 160° | 7.23 | −14.22 | 15.95 |
| 173° | 8.82 | −9.61 | 13.04 |
| 180° | 12.32 | −4.78 | 13.21 |
| 200° | 8.44 | −1.37 | 8.55 |
| 220° | 7.32 | 1.43 | 7.46 |
| 228° | 3.82 | 1.86 | 4.25 |
| 240° | 2.11 | 3.24 | 3.87 |
| 260° | 0.25 | 8.35 | 8.35 |
| 280° | −1.42 | 9.55 | 9.65 |
| 300° | −1.53 | 8.72 | 8.85 |
| 312° | −4.51 | 4.32 | 6.25 |
| 320° | −3.46 | 2.38 | 4.20 |
| 340° | −9.43 | 2.27 | 9.70 |

Figure 8 shows the polar coordinates location of the surface of the roadway versus the vertical displacement, horizontal displacement, and total displacement. Figure 8a, shows that the horizontal displacement is symmetrical with the calculation azimuth from 0° to 360°. While the vertical displacement shows an unsymmetrical trend, in which the displacement increases with the angle from 0° to 100° and 200° to 280°, the total displacement versus calculation azimuth is shown in Figure 8b. It can be seen the maximum deformation is at an angle of 100°. Figure 8c shows the geometric diagram after deformation, from which the deformation control should pay attention to the angle of 100°, 173°. Figure 8d is the on-site deformation of the roadway. It is clear that in the low side of position 100° to 180 ° there is a clear convergence, and a wood crib was employed to support the roof. In the high side wall there is a lack of free-standing support; thus, a clear side deformation is seen in Figure 8c.

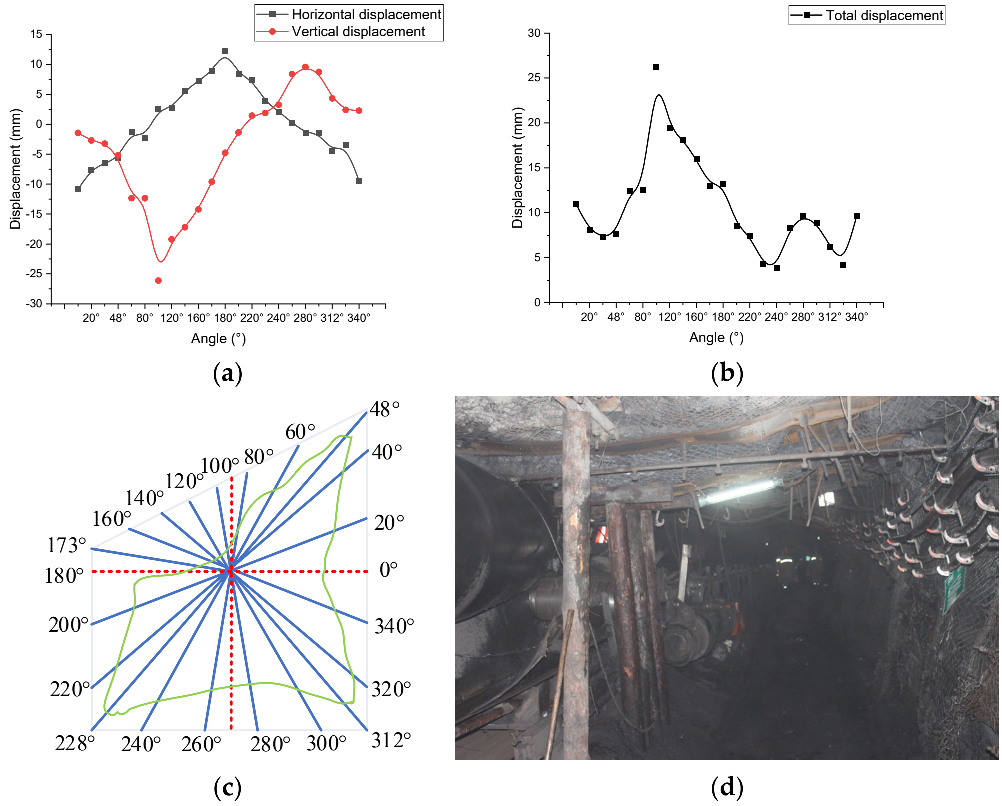


**Figure 8.** Calculation points versus displacement: (**a**) vertical displacement and horizontal displacement; (**b**) total displacement; (**c**) deformation geometric diagram; (**d**) on−site deformation results.

### 3.3.2. Stress Characteristics

The calculation stress results are shown in Table 2. From Table 2, both the horizontal and vertical stress concentrations occur at the four corners of the roadway, in the position of 48°, 60°, 173°, and 312°. The upper-left corner has the largest concentration, followed by the upper-right corner. In the upper-left corner, the wood crib can be installed for roof-to-floor support, while in the upper-right corner, there is a lack of free-standing support. Therefore, attention should be paid to the most damaged location to control the position in the upper-right corner.

**Table 2.** Stress results.

| Angle | $\sigma_x$/MPa | $\sigma_y$/MPa | Angle | $\sigma_x$/MPa | $\sigma_y$/MPa |
|---|---|---|---|---|---|
| 0° | 0 | −9.55 | 180° | 0 | −11.86 |
| 20° | 0 | −8.42 | 200° | 0 | −11.05 |
| 40° | 0 | −10.72 | 220° | 0 | −11.78 |
| 48° | −10.42 | −8.31 | 228° | −7.29 | −12.23 |
| 60° | −10.33 | −2.42 | 240° | −11.52 | 0 |
| 80° | −8.50 | −0.02 | 260° | −9.08 | 0 |
| 100° | −6.81 | −0.84 | 280° | −8.57 | 0 |
| 120° | −6.83 | −0.71 | 300° | −10.62 | 0 |
| 140° | −8.05 | −2.65 | 312° | −6.31 | −11.06 |
| 160° | −8.27 | −4.47 | 320° | 0 | −10.84 |
| 173° | −7.73 | −9.09 | 340° | 0 | −9.89 |

Figure 9 shows the stress distribution versus the calculation points. From Figure 9a, the vertical and horizontal stress shows the same trend as the calculation points. However, the stress distribution is quite complex compared with a circular and rectangular cross-section. Figure 9b,c clearly show that on the side of the corner, the horizontal and vertical stress concentration is in the corner. In addition, horizontal stress occurred on the roof and floor, which indicates the tension failure in this area. The vertical stress occurs in the two-side rib, this indicates that the vertical load bearing is carried by side coal. On the right side, Figure 9d shows the broken range on the upper corner on-site. Due to the lack of support, the upper corner on both sides is more likely to experience stress concentration, thus it is more likely to be broken, and attention should be paid to support in these areas.

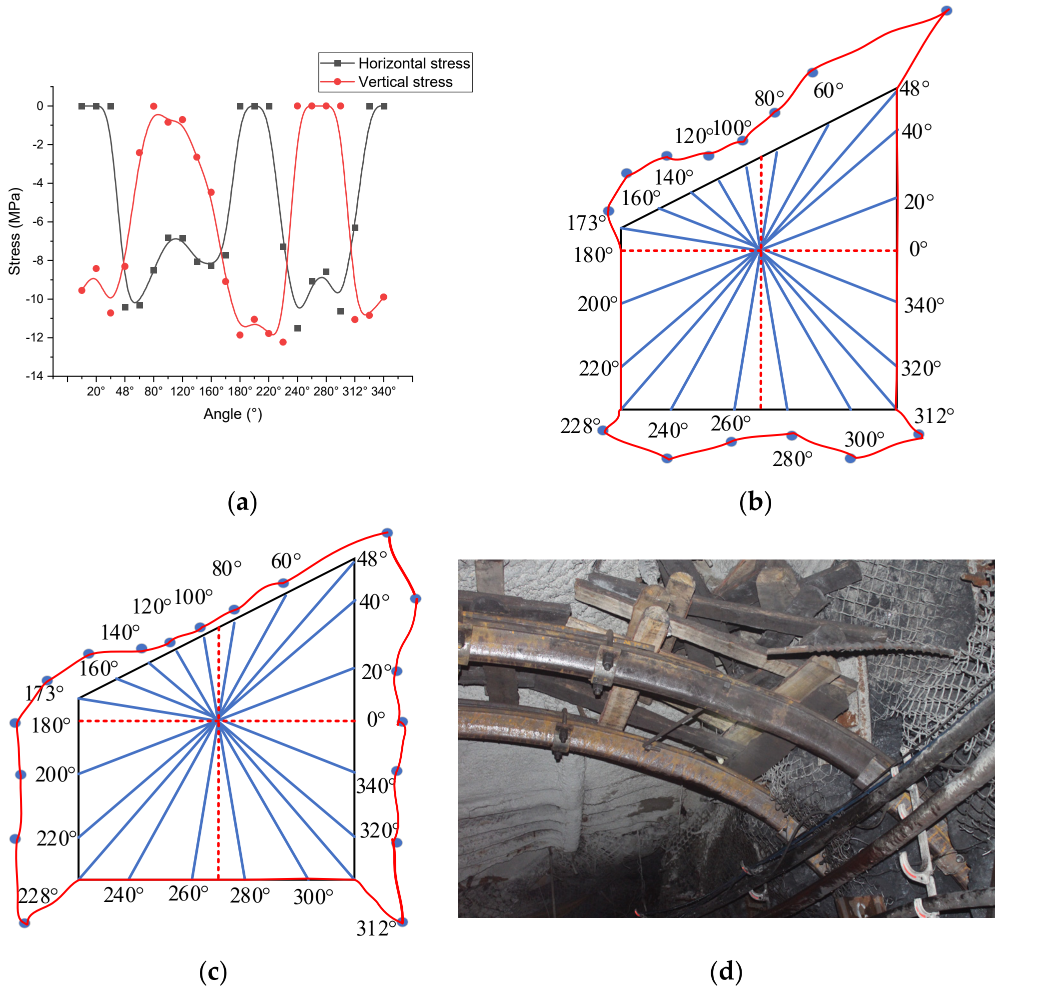


**Figure 9.** Stress calculation points versus stress: (**a**) vertical and horizontal stress versus angle; (**b**) horizontal stress distribution; (**c**) vertical stress distribution; (**d**) on−site upper corner broken range.

## 4. On-Site Experiment

### *4.1. The Yielding Prop Supporting Method Based on Stress and Deformation on the Trapezoidal Roadway*

Based on the analytical results on stress and deformation on the trapezoidal roadway, it can be concluded that: (1) The deformation of the high wall is larger than that of the low wall, and the deformation of the roof is larger than that of the floor. The overall deformation of the surrounding rock shows the rib closure is larger than the roof-to-floor closure. (2) The stress of surrounding rock shows that both horizontal and vertical stresses are maximum in the upper corner, indicating that the broken zone is most likely to occur at this location. Therefore, the supporting key location should be in the upper corner.

However, there are few efficient and effective supporting materials with constant high working resistance, with supporting length up to 4 m. A yielding prop with high load capacity and adjustable supporting height ranging from 1 m to 4.5 m was introduced by our previous studies [30,31]. The main schematic structure of the prop is shown in Figure 10, which is a compound apparatus consisting of three parts: an outer prop with an inner surface, an inner prop, and steel balls. The steel balls are uniformly located in the sloping ramp arrangement for setting the inner and outer props in place concerning each other. Due to the self-lock function of steel balls under gravity, tools are not required for installing the prop. The steel balls interlock between the inner and outer props, generating a reactive load. Therefore, the innovative prop is suitable to install on the upper side to support the roof and floor with constant working resistance.

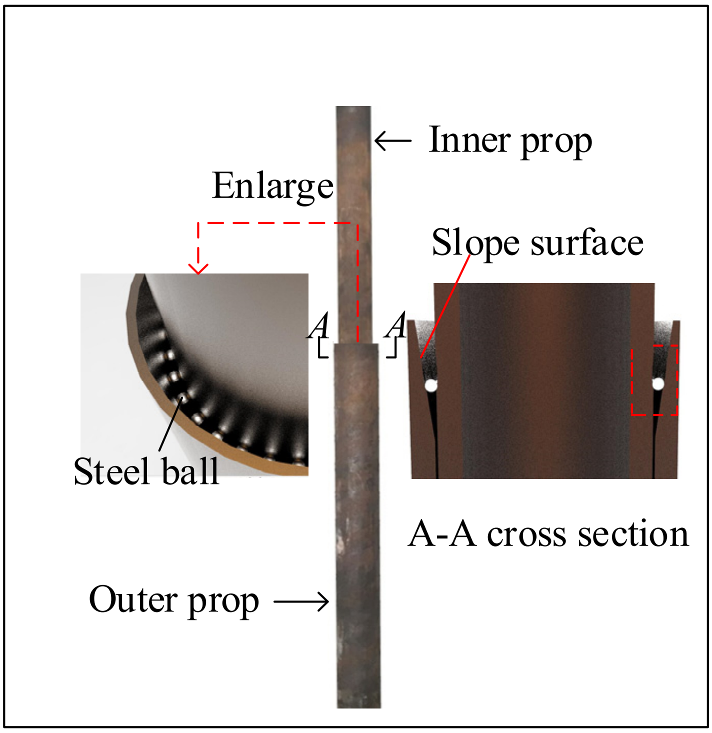


**Figure 10.** Diagram of yielding prop with high load capacity and adjustable supporting length.

*4.2. The On-Site Supporting Method with Yielding Prop*

According to the on-site drilling TV results on broken rock height, the loosening range was about 5 m. Therefore, the weight of the rock within the loosening circle is regarded as the weight to be supported by the high-yielding prop. The average weight of the roof rocks is 16 kN/m$^3$. Combined with the roadway width of 4 m, it was calculated that each 1 m length of the roadway needs to support a strength of about 400 kN. If only high-yielding props were employed, the density of the prop would be too large to meet pedestrians, ventilation, transportation, etc. To reduce the density of high-yielding props, cable was used to replace some high-yielding props, and high-strength plastic mesh and steel bands were employed to enhance the hanging effect on the cable. The specific supporting parameters are shown in Figure 11a: the row of the high-yielding prop with working resistance of 400 kN was set to 5 m, and the column distance was 1.6 m. The $\pi$-shaped beam was used to connect the roof, and the pillar boots were worn for it. Two anchor cables of 8.3 m in length and 21.8 mm in diameter were installed in the trapezoidal roof with a preload of 100 kN, a row spacing of 1000 mm, and a row spacing of 1600 mm; rock bolts of 2.4 m in length and 22 mm in diameter were used with a preload of 40 kN, a row spacing of 900 mm. Figure 11b shows the physical picture of the supporting.

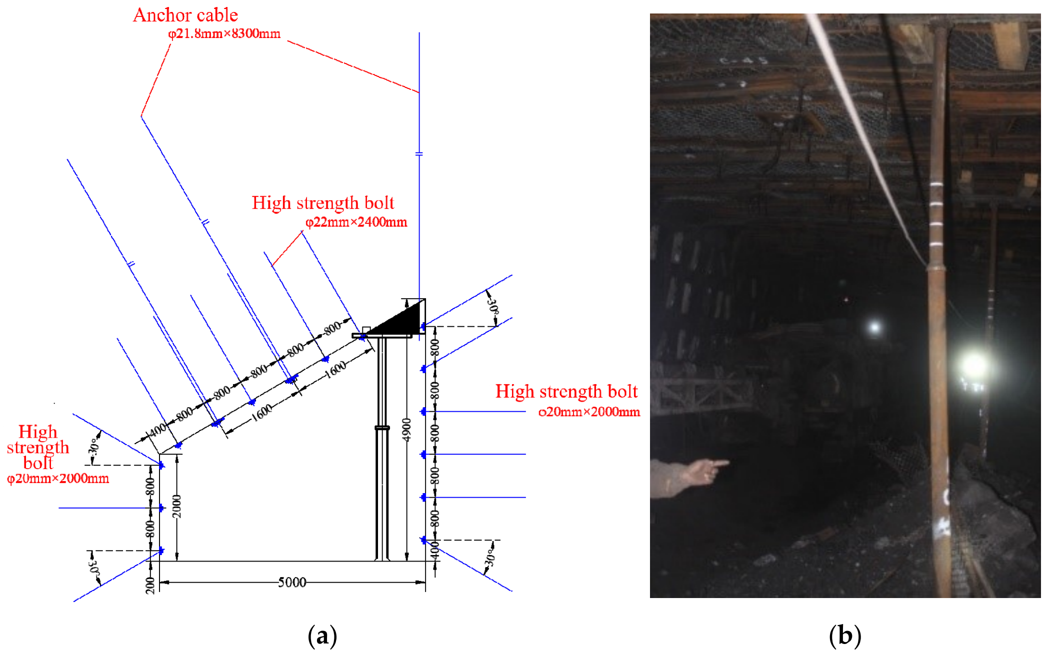


**Figure 11.** Schematic diagram of high-yielding prop in large inclination coal seam: (**a**) 5-1081 roadway diagram; (**b**) on-site application.

*4.3. Monitoring Method*

To evaluate the effect on the high-yielding prop support, deformation in the range of limestone of 350 m to 250 m was observed, as shown in Figure 12b. The monitoring parameters include roadway deformation, prop deformation, and rock bolt axial force. These three parameters are described in detail below: (1) Roadway deformation: The cross-point method is used to observe the deformation of the convergence of the rib side and roof to the floor as shown in Figure 12a. (2) Prop shrinkage: The prop shrinkages were used to reflect the supporting effect referenced to its load–displacement curve. Therefore, along the 5-1081 roadway, the radial deformation of the outer prop and shrinkage were counted every 20 m within the range of 350 m to 250 m of the limestone level. (3) Rock bolt axial force: The rock bolt axial force in the 5-1081 roadway was tested by nondestructive testing techniques developed by our group. The axial force variation is positive, corresponding to the stability of the roadway; therefore, the first observation point was arranged from within 347.8 m of the mining level, and a measurement point was arranged every 5 m.

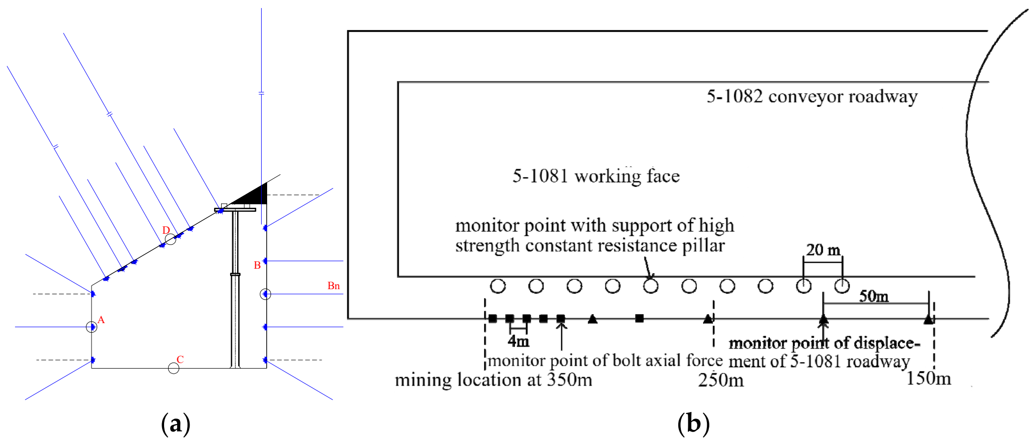


**Figure 12.** Measuring point location of 5-1081 roadway: (**a**) measurement point on roadway cross-section diagram; (**b**) layout diagram of the monitoring points.

### 4.4. Test Results

#### 4.4.1. Roadway Deformation

For the convergence comparison between the original method and the high-yielding support method shown in Figure 13, under the original support condition, the floor heaven is 800 mm~1300 mm in the range of 40–50 m ahead of the roadway. Under the condition using a high-yielding prop, the maximum floor heaven of the roadway is 800 mm, and the limestone reaches 800 mm in the range of only 10 m ahead of the roadway. The range of floor heaven is reduced, and the floor heaven difference is about 250 mm, which effectively proves that the high-yielding prop controls the floor heaven. At the same time, the floor deformation was reduced from the maximum value of 570 mm to 420 mm, and the range affected by mining was reduced by about 20 m. The deformation of the two ribs was also reduced from the maximum value of 320 mm to 210 mm. From the analysis of the practical effect of the supporting, the high-yielding prop greatly reduces the floor rock deformation in the upper corner of the trapezoidal roadway. Under the influence of mining disturbance, the deformations at the top corner decreased by 40% compared with before. These observation results show that the new yielding support is effective to control roadway deformation.

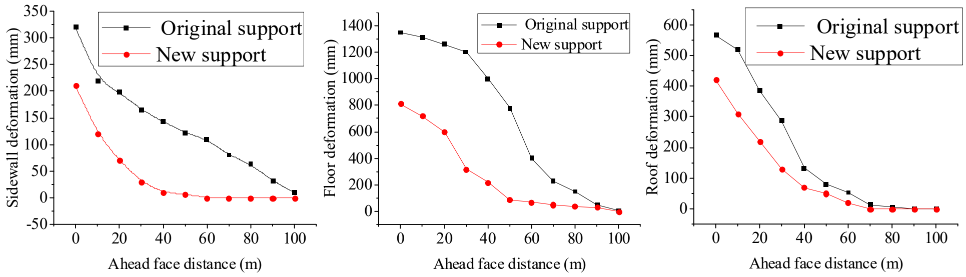


**Figure 13.** Convergence comparison between original method and high yieldable support method.

#### 4.4.2. Prop Shrinkage

From the deformation characteristics of the roadway, we can calculate that the range of the over-support pressure generated by mining is about 100 m. Therefore, we selected the prop shrinkage range at 100 m and 40 m ahead of the working face. As shown in Figure 14, both props produced radial expansion. With a distance from 100 m to 40 m, the inner prop shows an obvious shrinkage. According to the laboratory test results, the designed maximum working resistance was reached at this time. It indicates the prop can support the roof shrinkage at a stable load.

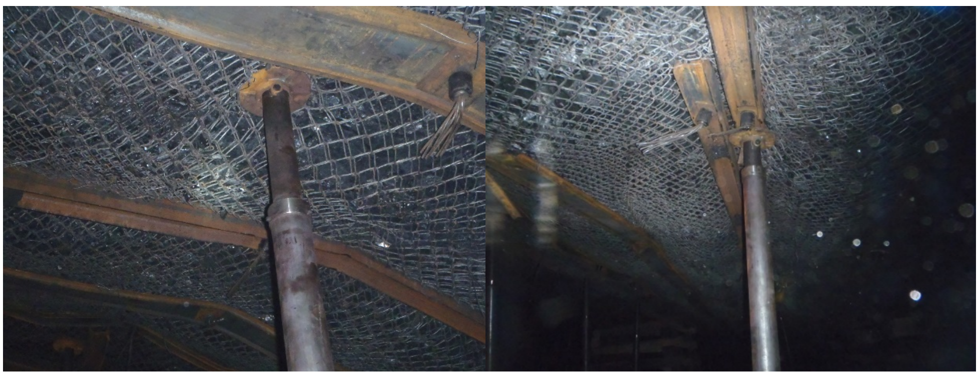

(**a**) (**b**)

**Figure 14.** Shrinkage distance with a time of high load capacity and yieldable prop: (**a**) ahead face 100 m; (**b**) ahead face 40 m.

### 4.4.3. Rock Bolt Axial Force

Figure 15 shows the rock bolt axial forces versus the working face distance on original supports and new supports. It is clearly shown that the axial forces decrease at a range of 5 kN to 26 kN. In the position on the ahead face 10 m, the axial force differences reach the maximum value of 26 kN, which indicates the maximum deformation range. After this position, the differences become general, which indicates the slow deformation of rocks after the ahead face distance of 10 m.

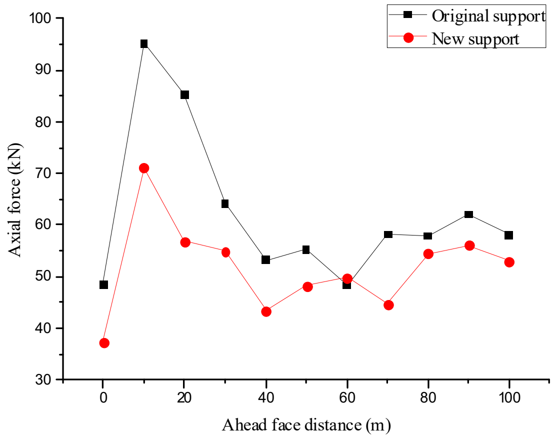


**Figure 15.** The bolt axial force comparison between the original supporting method and high yieldable supporting method.

## 5. Conclusions

There is still a lack of systematic research on stress and deformation on the surrounding rock of large, inclined coal seam roadways; thus, a blind and efficient supporting method. In this paper, an analytical solution employed with complex analysis and comfort map is solved to obtain stress and deformation on surrounding rocks of the trapezoidal roadway. Then, based on the analytical results, the high-yielding prop was employed as innovative supporting materials, and the on-site experiments were conducted. The main results are as follows:

(1) The horizontal displacement is symmetrical with the calculation azimuth from 0° to 360°. While the vertical displacement shows an unsymmetrical trend, in which the displacement increases with the angle from 0° to 100° and 200° to 280°. The maximum total deformation is at the angle of 100°. The deformation control should pay attention to the angle of 100°, 173°.

(2) The vertical and horizontal stress shows the same trend versus the azimuth. However, the stress distribution is quite complex compared with a circular and rectangular cross-section.

(3) The deformation of the high wall is larger than that of the low wall, and the deformation of the roof is larger than that of the floor. The overall deformation of the surrounding rock shows the rib closure is larger than the roof-to-floor closure. The stress of the surrounding rock shows that both horizontal and vertical stresses are maximum in the upper corner, indicating that the broken zone is most likely to occur at this location. Therefore, the supporting key location should be in the upper corner.

(4) A novel yielding prop with a constant working resistance was employed to install on the upper side to support the roof and floor. The roadway deformation, prop shrinkage, and rock bolt axial forces show that the high-yielding prop not only controls the deformation effectively but is also more convenient and environmentally friendly.

**Author Contributions:** Conceptualization, Y.H., Y.W. and C.L.; methodology, Y.H. and K.Z.; software, C.L.; validation, Y.H. and Y.W.; formal analysis, Y.H.; investigation, L.S.; resources, K.Z.; data curation, H.P.; writing—original draft preparation, Y.H. and L.S.; writing—review and editing, Y.W.;

visualization, Y.H.; supervision, Y.W.; project administration, Y.W.; funding acquisition. All authors have read and agreed to the published version of the manuscript.

**Funding:** This research was funded by the National Natural Science Foundation of China (No.51674247, No.52204114, No.52104101) and the Natural Science Foundation of Jiangsu Province (BK20210522).

**Data Availability Statement:** Not applicable.

**Acknowledgments:** We thank the funding by the National Natural Science Foundation of China (No.51674247, No.52204114, No.52104101) and the Natural Science Foundation of Jiangsu Province (BK20210522).

**Conflicts of Interest:** The authors declare no conflict of interest.

## References

1. He, S.Q.; Song, D.Z.; Li, Z.L.; He, X.Q.; Chen, J.Q.; Li, D.H.; Tian, X.H. Precursor of Spatio-temporal Evolution Law of MS and AE Activities for Rock Burst Warning in Steeply Inclined and Extremely Thick Coal Seams Under Caving Mining Conditions. *Rock Mech. Rock Eng.* **2019**, *52*, 2415–2435. [CrossRef]
2. Carroll, T.; Ho, C.; Richards, T.; Torres, J. Design and Construction of a Soil Cement Mixed TBM Retrieval Shaft in Porous Limestone. *Grouting* **2017**, 269–278. [CrossRef]
3. Li, S.; Zheng, C.; Zhao, Y. Numerical Modeling on Blasting Stress Wave in Interbedding Rheological Rockmass for the Stability of the Main Shaft of Mine. *Front. Earth Sci.* **2022**, *10*, 930013. [CrossRef]
4. Chen, C.; Zhou, J.; Zhou, T.; Yong, W.X. Evaluation of vertical shaft stability in underground mines: Comparison of three weight methods with uncertainty theory. *Nat. Hazards* **2021**, *109*, 1457–1479. [CrossRef]
5. Long, L.L.; Liu, Y.; Chen, X.Y.; Guo, J.T.; Li, X.H.; Guo, Y.N.; Zhang, X.Y.; Lei, S.G. Analysis of Spatial Variability and Influencing Factors of Soil Nutrients in Western China: A Case Study of the Daliuta Mining Area. *Sustainability* **2022**, *14*, 2793. [CrossRef]
6. Zhang, H.D.; Hu, G.Z.; Zhao, G.C. Research on the Movement Law of Roof Structure in Large-Inclined Coal Seam Working Face: A Case Study in Liu.Pan.Shui. Mining Area. *Shock Vib.* **2022**, 6328851. [CrossRef]
7. Xia, Y.Q.; Wang, X.Q.; Li, H.Z.; Li, W. China's Provincial Environmental Efficiency Evaluation and Influencing Factors of the Mining Industry Considering Technology Heterogeneity. *IEEE Access* **2020**, *8*, 178924–178937. [CrossRef]
8. Zeng, Q.; Dong, J.X.; Zhao, L.H. Investigation of the potential risk of coal fire to local environment: A case study of Daquanhu coal fire, Xinjiang region, China. *Sci. Total Environ.* **2018**, *640*, 1478–1488. [CrossRef]
9. Liu, W.T.; Mu, D.R.; Xie, X.X.; Yang, L.; Wang, D.H. Sensitivity Analysis of the Main Factors Controlling Floor Failure Depth and a Risk Evaluation of Floor Water Inrush for an Inclined Coal Seam. *Mine Water Environ.* **2018**, *37*, 636–648. [CrossRef]
10. Wang, Z.Q.; Liu, C.S.; Wu, J.D.; Jiang, H.S.; Zhao, Y.M. Impact of screening coals on screen surface and multi-index optimization for coal cleaning production. *J. Clean. Prod.* **2018**, *187*, 562–575. [CrossRef]
11. Sun, X.Y.; Ho, C.H.; Li, C.; Xia, Y.C.; Zhang, Q. Inclination effect of coal mine strata on the stability of loess land slope under the condition of underground mining. *Nat. Hazards* **2020**, *104*, 833–852. [CrossRef]
12. Ren, W.X.; Shi, J.T.; Zhu, J.T.; Guo, Q. An innovative dust suppression device used in underground tunneling. *Tunn. Undergr. Space Technol.* **2020**, *99*, 103337. [CrossRef]
13. Qi, X.Y.; Wang, R.J.; Mi, W.T. Failure Characteristics and Control Technology of Surrounding Rock in Deep Coal Seam Roadway with Large Dip Angle under the Influence of Weak Structural Plane. *Adv. Civ. Eng.* **2020**, 6623159. [CrossRef]
14. Wang, Y.L.; Tang, J.X.; Dai, Z.Y.; Yi, T.; Li, X.Y. Flexible roadway protection technology in medium-thickness coal seam with large dip angle. *Energy Source Part A Recover. Util. Environ. Eff.* **2019**, *41*, 3085–3102. [CrossRef]
15. Hu, K.; Yao, Z.S.; Wu, Y.S.; Xu, Y.J.; Wang, X.J.; Wang, C. Application of FBG Sensor to Safety Monitoring of Mine Shaft Lining Structure. *Sensors* **2022**, *22*, 4838. [CrossRef]
16. Xie, F.X. Control of Gob-Side Roadway with Large Mining Height in Inclined Thick Coal Seam: A Case Study. *Shock Vib.* **2021**, *2021*, 6687244.
17. Khodadadian, A.; Noii, N.; Parvizi, M.; Abbaszadeh, M.; Wick, T.; Heitzinger, C. A Bayesian estimation method for variational phase-field fracture problems. *Comput. Mech.* **2020**, *66*, 827–849. [CrossRef]
18. Ren, C.; Yu, J.; Liu, S.; Yao, W.; Zhu, Y.; Liu, X. A Plastic Strain-Induced Damage Model of Porous Rock Suitable for Different Stress Paths. *Rock Mech. Rock Eng.* **2022**, *55*, 1887–1906. [CrossRef]
19. Yu, J.; Zhu, Y.; Yao, W.; Liu, X.; Ren, C.; Cai, Y.; Tang, X. Stress relaxation behaviour of marble under cyclic weak disturbance and confining pressures. *Measurement* **2021**, *182*, 109777. [CrossRef]
20. Xu, Z.; Li, X.; Li, J.; Xue, Y.; Jiang, S.; Liu, L.; Luo, Q.; Wu, K.; Zhang, N.; Feng, Y. Characteristics of Source Rocks and Genetic Origins of Natural Gas in Deep Formations, Gudian Depression, Songliao Basin, NE China. *ACS Earth Space Chem.* **2022**, *6*, 1750–1771. [CrossRef]
21. Li, J.; Wang, Y.; Nguyen, X.; Zhuang, X.; Li, J.; Querol, X.; Li, B.; Moreno, N.; Hoang, V.; Cordoba, P. First insights into mineralogy, geochemistry, and isotopic signatures of the Upper Triassic high-sulfur coals from the Thai Nguyen Coal field, NE Vietnam. *Int. J. Coal Geol.* **2022**, *261*, 104097. [CrossRef]

22. Zhang, J.H.; Chen, H.; Shi, X.Z.; Guan, W.M.; Sun, X.L. Research on Stress Distribution Characteristics for Uniquely Shaped Roadway with Hard Roof in Steeply Inclined Coal Seam and Support Technology of Reducing Vibration Impact. *Shock Vib.* **2021**, *2021*, 2785479. [CrossRef]
23. Chen, B.; Zuo, Y.J.; Zheng, L.L.; Zheng, L.J.; Lin, J.Y.; Pan, C.; Sun, W.J.B. Deformation failure mechanism and concrete-filled steel tubular support control technology of deep high-stress fractured roadway. *Tunn. Undergr. Space Technol.* **2022**, *129*, 104684. [CrossRef]
24. Yang, R.S.; Li, Y.L.; Guo, D.M.; Yao, L.; Yang, T.M.; Li, T.T. Failure mechanism and control technology of water-immersed roadway in high-stress and soft rock in a deep mine. *Int. J. Min. Sci. Technol.* **2017**, *27*, 245–252. [CrossRef]
25. Tan, X.J.; Chen, W.Z.; Liu, H.Y.; Chan, A.H.C.; Tian, H.M.; Meng, X.J.; Wang, F.Q.; Deng, X.L. A combined supporting system based on foamed concrete and U-shaped steel for underground coal mine roadways undergoing large deformations. *Tunn. Undergr. Space Technol.* **2017**, *68*, 196–210. [CrossRef]
26. Wang, M.Y.; Lin, T.S.; Yin, L.J.; Yang, Y.; Yang, L. Research on Roadway Surrounding Rock Control Technology Using O-arch Combination Support Scheme. In Proceedings of the 3rd International Conference on Advances in Energy and Environmental Science, Zhuhai, China, 25–26 July 2015; Volume 31, pp. 865–870.
27. Yang, Z.Q.; Liu, C.; Tang, S.C.; Dou, L.M.; Cao, J.L. Rock burst mechanism analysis in an advanced segment of gob-side entry under different dip angles of the seam and prevention technology. *Int. J. Min. Sci. Technol.* **2018**, *28*, 891–899. [CrossRef]
28. Kong, J.; Chen, P.; Chen, J.; Liu, Q.S.; Ma, Z. Research on support technology in deep roadway of Huafeng mine. *Adv. Mater. Res.* **2013**, *753–755*, 831–834. [CrossRef]
29. Dong, X.J.; Karrech, A.; Basarir, H.; Elchalakani, M.; Qi, C.C. Analytical solution of energy redistribution in rectangular openings upon insitu rock mass alteration. *Int. J. Rock Mech. Min. Sci.* **2018**, *106*, 74–83. [CrossRef]
30. Hao, Y.; Wu, Y.; Chen, L.; Teng, Y. An innovative yielding prop with high stable load capacity and long shrinkage distance in coal mine. *Mech. Adv. Mater. Struct.* **2019**, *26*, 1568–1579. [CrossRef]
31. Hao, Y.; Wu, Y.; Chen, Y.L.; Li, P.; Chen, L.; Zhang, K. An innovative equivalent width supporting technology for sustaining large-cross section roadway in thick coal seam. *Arab. J. Geosci.* **2019**, *12*, 688. [CrossRef]